Pharmacokinetic Assessment of the Uptake of 16β-^{18}F-Fluoro-5α-Dihydrotestosterone (FDHT) in Prostate Tumors as Measured by PET

Bradley J. Beattie*[1], Peter M. Smith-Jones*[2], Yuliya S. Jhanwar[3], Heiko Schöder[2], C. Ross Schmidtlein[4], Michael J. Morris[5], Pat Zanzonico[4], Olivia Squire[2], Gustavo S.P. Meirelles[6], Ron Finn[2], Mohammad Namavari[7], Shangde Cai[2], Howard I. Scher[5], Steven M. Larson[2], and John L. Humm[4]

[1]Department of Neurology, Memorial Sloan-Kettering Cancer Center, New York, New York; [2]Department of Radiology, Memorial Sloan-Kettering Cancer Center, New York, New York; [3]Department of Radiology, St. Luke's-Roosevelt Hospital, New York, New York; [4]Department of Medical Physics, Memorial Sloan-Kettering Cancer Center, New York, New York; [5]Genitourinary Oncology Service, Department of Medicine, Memorial Sloan-Kettering Cancer Center, New York, New York; [6]Department of Radiology, Federal University of São Paulo, São Paulo, Brazil; and [7]Department of Radiology and Bioengineering, Bio-X Program, Stanford University, Stanford, California

The aim of this study was to develop a clinically applicable noninvasive method to quantify changes in androgen receptor (AR) levels based on ^{18}F-16β-fluoro-5α-dihydrotestosterone (^{18}F-FDHT) PET in prostate cancer patients undergoing therapy. **Methods:** Thirteen patients underwent dynamic ^{18}F-FDHT PET over a selected tumor. Concurrent venous blood samples were acquired for blood metabolite analysis. A second cohort of 25 patients injected with ^{18}F-FDHT underwent dynamic PET of the heart. These data were used to generate a population-based input function, essential for pharmacokinetic modeling. Linear compartmental pharmacokinetic models of increasing complexity were tested on the tumor tissue data. Four suitable models were applied and compared using the Bayesian information criterion (BIC). Model 1 consisted of an instantaneously equilibrating space, followed by a unidirectional trap. Models 2a and 2b contained a reversible space between the instantaneously equilibrating space and the trap, into which metabolites were excluded (2a) or allowed (2b). Model 3 built on model 2b with the addition of a second reversible space preceding the unidirectional trap and from which metabolites were excluded. **Results:** The half-life of the ^{18}F-FDHT in blood was between 6 and 7 min. As a consequence, the uptake of ^{18}F-FDHT in prostate cancer lesions reached a plateau within 20 min as the blood-borne activity was consumed. Radiolabeled metabolites were shown not to bind to ARs in in vitro studies with CWR22 cells. Model 1 produced reasonable and robust fits for all datasets and was judged best by the BIC for 16 of 26 tumor scans. Models 2a, 2b, and 3 were judged best in 7, 2, and 1 cases, respectively. **Conclusion:** Our study explores the clinical potential of using ^{18}F-FDHT PET to estimate free AR concentration. This process involved the estimation of a net uptake parameter such as the k_{trap} of model 1 that could serve as a surrogate measure of AR expression in metastatic prostate cancer. Our initial studies suggest that a simple body mass–normalized standardized uptake value correlates reasonably well to model-based k_{trap} estimates, which we surmise may be proportional to AR expression. Validation studies to test this hypothesis are underway.

Key Words: molecular imaging; PET/CT; radiotracer tissue kinetics; FDHT; dynamic PET; pharmacokinetic modeling; prostate cancer

J Nucl Med 2010; 51:183–192
DOI: 10.2967/jnumed.109.066159

The androgen receptor (AR) is known to be important in the development and progression of prostate cancer. Castration-resistant prostate cancers in particular harbor a series of oncogenic alterations in AR including overexpression, increased copy number, mutations that affect ligand specificity, and an increase in the enzyme levels responsible for antigen synthesis (*1*). It is for this reason that there is increasing interest in the development of therapies directed at these alterations.

Currently, a direct biopsy of a metastatic lesion is required to assess the AR status in tumors when treatment is being considered. Although technically feasible, this procedure is invasive, costly, not a part of routine practice, and difficult to repeat. Moreover, the AR status determined histopathologically in one metastasis may not be representative of all metastatic lesions.

A PET ligand that could provide a signal that is predictive of AR expression levels in prostate cancer not only would have great potential in the diagnosis of this disease but also could have implications in determining the

Received Jul. 27, 2009; revision accepted Oct. 7, 2009.
For correspondence or reprints contact: John L. Humm, Memorial Sloan-Kettering Cancer Center, 1275 York Ave., New York, NY 10021.
E-mail: hummj@mskcc.org
*Contributed equally to this work.

appropriate therapy and in assessing its efficacy. This is especially pertinent in an era when targeted therapies are becoming available clinically, as molecular imaging approaches can potentially be used to select patients likely to respond to such therapies and to monitor the therapeutic effectiveness of these treatments.

^{18}F-16β-fluoro-5α-dihydrotestosterone (^{18}F-FDHT) is a structural analog of 5α-dihydrotestosterone (DHT), the principal intraprostatic form of androgen (*2*). Among fluorinated androgen analogs studied in animals, ^{18}F-FDHT uptake in the prostate was blocked (reduced ~10-fold) by the coadministration of cold testosterone and yielded the highest levels of unmetabolized radioligand in blood up to 45 min after injection and the highest prostate-to-bone and prostate-to-muscle activity concentration ratios up to 4 h after injection. Thus, ^{18}F-FDHT appears to bind specifically to ARs in vivo and to have the most favorable targeting properties for noninvasive imaging among AR-binding radiotracers studied to date. In addition, like androgens generally, most of the ^{18}F-FDHT in circulation is bound to sex hormone–binding globulin (*3*). Such plasma–protein binding presumably serves to retard degradation of endogenous androgens and to facilitate their transport into cells. These considerations led to the selection of ^{18}F-FDHT as the lead radiopharmaceutical for further evaluation in clinical studies. Two clinical studies subsequently demonstrated successful PET of prostate cancer using ^{18}F-FDHT (*4–6*). These studies showed rapid tumor uptake and systemic metabolism of ^{18}F-FDHT and provided some evidence that the foci of activity seen on ^{18}F-FDHT PET images correlates with AR-expressing tissue as demonstrated by immunohistochemical staining. In this article, we describe our initial investigations seeking to use pharmacokinetic modeling of ^{18}F-FDHT time–activity data in prostate tumors, as measured by dynamic PET, to assess relative levels of AR in such tumors.

MATERIALS AND METHODS

Patients

Patients were selected prospectively under the auspices of the Memorial Sloan-Kettering Cancer Center Institutional Review Board (protocol 00-095). All who agreed to participate in the study signed informed consent forms. The study cohort consisted of 13 patients who then underwent dynamic ^{18}F-FDHT PET over a selected metastatic tumor site, located in either the pelvis or the abdomen. Because satisfactory region-of-interest (ROI)–based blood time–activity data (i.e., input functions) could not, in general, be obtained from these images, arterial input data were extracted from a larger cohort of 25 patients, who underwent dynamic ^{18}F-FDHT PET of the heart. Data from ROIs placed over the aorta in these patients were averaged to generate a population-based input function used in the pharmacokinetic modeling.

For the 13 patients recruited into the first cohort, there were a total of thirty ^{18}F-FDHT scans obtained, consisting of 3 patients for whom a single ^{18}F-FDHT baseline scan only was obtained, 3 patients for whom 1 pre- and 1 posttherapy ^{18}F-FDHT scan were obtained, and 7 patients for whom a baseline scan followed by 2 posttherapy scans were obtained.

Radiochemical Synthesis of ^{18}F-FDHT

^{18}F-FDHT was synthesized as previously described (*5*). The total radiochemistry synthesis time was approximately 100 min, and the radiochemical yield to end of bombardment was nearly 30%. Chemical and radiochemical quality assurance (QA) was performed by radio–thin-layer chromatography and reversed-phase high-performance liquid chromatography (HPLC) by coelution with a fully characterized nonradioactive standard. Additional QA included confirmation of color, appearance, radioactive half-life, pH, sterility, and apyrogenicity. All QA results were in full accordance with the approved specifications. The radiochemical purity was greater than 99%.

To maintain the chemical stability of the ^{18}F-FDHT compound, the final product was formulated in a 5% ethanol solution, precluding the use of a bolus injection because of the burning sensation at the injection site associated with the intravenous administration of alcohol. As a consequence, injections were manually performed using a lead-shielded syringe for 40 s to 2 min, and the rate was reduced based on patient feedback.

Binding Studies with ^{18}F-FDHT

Displacement studies were performed with ^{18}F-FDHT and CWR22-rv1 cells with FDHT and DHT as competitors. Briefly, triplicate samples of cells were mixed with 20,000 counts per minute of ^{18}F-FDHT and increasing amounts of cold competitor (1 pM to 1 μM). The solutions were then shaken on an orbital shaker at ambient temperature, and after 60 min the cells were isolated and washed with ice-cold Tris-buffered saline using a M-24T cell harvester (Brandel). All of the isolated cell samples were counted, with appropriate standards of total activity and blank controls, and the specific uptake of ^{18}F-FDHT determined. These data were plotted against the concentration of the cold competitor to give sigmoidal displacement curves (Fig. 1). The inhibitory concentration of 50% was determined using a 1-site model and a least-squares curve-fitting routine (Origin; OriginLab). The r^2 of the curve fit was 0.99.

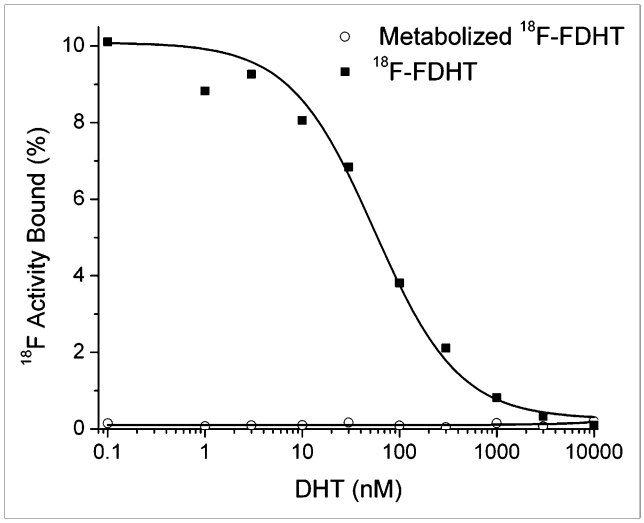

FIGURE 1. Displacement binding of ^{18}F-FDHT and final ^{18}F-FDHT metabolite to CWR22-rv1 cells by DHT.

A sample of ^{18}F-FDHT drug product was evaporated to remove the ethanol and mixed with a 10% suspension of rat liver homogenate in phenazine methosulfate for 30 min at 37°C. At the end of this period, the solution was diluted to 40% acetonitrile and the precipitated proteins pelleted by centrifugation. The metabolized ^{18}F-FDHT supernatant was then purified by reversed-phase HPLC (C_{18} Ultrasphere column [Beckman]; 5 μm, 250 × 4.6 mm) using an gradient elution of 40% acetonitrile/10 mM phosphoric acid up to 90% acetonitrile/10 mM phosphoric acid over 10 min at a flow rate of 1 mL/min. Under these conditions, ^{18}F-FDHT elutes at around 8 min, and the main metabolite elutes at 4 min. The purified metabolite was then used in a displacement binding study as described above.

PET

Each patient underwent at least 1 whole-body ^{18}F-FDG PET/CT scan that was followed within 1–7 d by dynamic and whole-body ^{18}F-FDHT PET scans. The initial ^{18}F-FDG PET/CT scan was used to identify one or more lesions to be followed in the subsequent dynamic ^{18}F-FDHT scans. A subset of the patients received up to 2 additional sets of scans, approximately 4 and 12 wk later during their course of treatment.

All studies were performed on either a Discovery LS or an Advance PET scanner (GE Healthcare). Before the ^{18}F-FDG scans, patients were required to fast for at least 6 h and a blood sample was obtained to measure the serum glucose level. No fasting was required for the ^{18}F-FDHT scan. For all ^{18}F-FDHT scans, each patient had 1 peripheral intravenous line placed into each arm, 1 for injection and 1 for blood sampling. Scanning in all cases was performed in 2-dimensional mode (septa-in).

The dynamic ^{18}F-FDHT PET emission scan was initiated coincident with the start of the injection. The first 2 patients underwent a dynamic scan of 55 min. Analysis of this dynamic imaging data, along with plasma metabolite analysis, showed little to no change in activity levels in the tumor occurring beyond 20 min after injection and almost complete metabolism of the compound. The protocol was, therefore, modified for patients 3–13, reducing the duration of the dynamic PET scan to 30 min. After the dynamic scan, patients were allowed to dismount from the table to rest for approximately 10 min. Patients were encouraged to urinate before the acquisition of a whole-body PET scan, which was used to determine overall biodistribution and to explore other potential metastatic sites. The whole-body scan was obtained from the skull base to the pelvic floor. All images were reconstructed using both filtered backprojection (FBP) and iterative reconstruction.

The 25 patients from the second cohort underwent an almost identical scan procedure, except that the 30-min dynamic scan was obtained over the chest to include the heart rather than over a metastatic index lesion. ROI data were derived from the aorta of these patients and were used to generate a population average input function for ^{18}F-FDHT.

Radiometabolite Analysis of ^{18}F-FDHT

Patients who underwent ^{18}F-FDHT scans had blood samples drawn to determine the clearance of ^{18}F-FDHT and the rate of metabolite formation. Blood samples were drawn at all or some of the following time points after injection with ^{18}F-FDHT: 1, 2, 3, 4, 5, 6, 7, 8, 9, 10, 15, 20, 25, 30, 40, and 50 min. Patients who underwent 30-min dynamic scans did not have the 40- and 50-min blood samples drawn, but whenever possible a blood sample was drawn at a late time point after the whole-body PET scan was obtained. The activities in whole blood, plasma, 30-kDa filtered plasma, and acetonitrile-precipitated plasma were determined. In addition, the relative amounts of ^{18}F-FDHT and ^{18}F-FDHT metabolites in the plasma were determined by HPLC.

Aliquots of whole blood were transferred to preweighed tubes. Portions of the blood samples were centrifuged and aliquots of plasma transferred into preweighed tubes. The remaining plasma samples underwent ultrafiltration using 30-kDa spin filters (Centricon YM-30; Millipore), and aliquots of the filtrate were transferred to preweighed tubes. ^{18}F activity in all samples was assayed in a γ-counter (LKB Wallac 1282; Compugamma) calibrated for ^{18}F, corrected for decay to the time of injection, and expressed as a percentage of the injected dose per gram.

The counted plasma samples were mixed with 0.45 mL of acetonitrile containing unlabeled FDHT (0.05 mg/mL) as a reference compound. After centrifugation at 2,000*g* for 5 min, the precipitated proteins were also counted in a γ-counter. The protein-free supernatant was analyzed by reversed-phase C_{18} HPLC. The Shimadzu HPLC system consisted of 2 LC10AT pumps and a SCL10A controller coupled to a SPD-10A ultraviolet detector and a Packard Radiometric 625TR flow detector (500 μL/cell, with bismuth germanate crystals) in series. The reversed-phase C_{18} column (Ultrasphere [Beckman]; 5 μm, 250 × 4.6 mm) was eluted, applying a gradient from 40% acetonitrile/10 mM phosphoric acid to 90% acetonitrile/10 mM phosphoric acid over 10 min at a flow rate of 1 mL/min. Under these conditions, ^{18}F-FDHT elutes at around 8 min and the main metabolized product at 4 min. The data were expressed as a percentage of the total activity in plasma.

ROI Analysis

One nuclear medicine reader analyzed the ROIs in this investigation. The tumor was identified by displaying the ^{18}F-FDG PET/CT scan alongside the whole-body ^{18}F-FDHT and regional dynamic ^{18}F-FDHT scans. Separate ROIs circumscribing a homogeneous region well within the borders of the index tumor were drawn on images from a summed frame, iteratively reconstructed, covering the last 15 min of the ^{18}F-FDHT PET emission data. ROIs were also generated for the descending aorta (3 studies in 2 patients) or iliac arteries (20 studies in 9 patients) using summed frames covering the first 2 min after ^{18}F-FDHT injection. All ROIs were applied to FBP-reconstructed images to generate curves of mean activity concentration versus time. FBP images were used here to avoid problems associated with spatially variant convergence rates encountered with iterative reconstruction methods. Multiple ROIs were weighted (by their fractional volume) and summed for structures extending over several adjacent images.

Because of the relatively large diameter of the descending aorta, we chose the 3 curves, so derived, as the reference against which to judge the accuracy of the iliac artery–derived curves and the venous blood samples. A comparison of the blood time–activity curves both within and among studies suggested that data from the venous blood samples and from ROIs drawn over the iliac arteries likely do not accurately represent the true blood–activity time course at early times after ^{18}F-FDHT injection. Only time–activity curves generated from ROIs drawn over the descending aorta showed the expected first-pass peak (Fig. 2). At late times (>15 min) all curves tended to plateau, with the aorta-derived and venous blood–derived data reaching approximately the same activity concentration level.

The descending aorta was within the field of view for only 2 patients in the first cohort; therefore, it was decided to use data

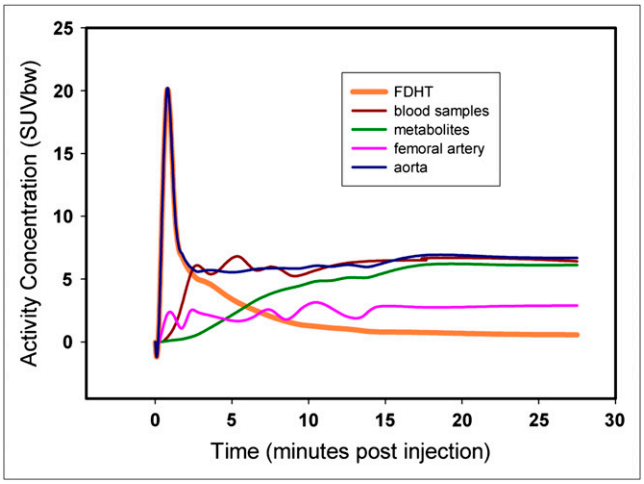

FIGURE 2. Time–activity curves in SUV units for blood samples (total, ^{18}F-FDHT and metabolites) and PET-derived data from iliac artery and aorta. SUV_{bw} = SUV normalized by body weight.

from a second separate cohort of patients for which dynamic PET scans of ^{18}F-FDHT were obtained over the heart. These data were used to establish a population-based blood time–activity curve. Curves derived from ROIs drawn over the aorta from this cohort of 25 patients were converted to standardized uptake values (SUVs = tissue activity per kg divided by injected activity per kg of body weight) and averaged. Individual radiolabeled metabolite and parent ^{18}F-FDHT input functions were calculated for each patient by first scaling the population-based blood time–activity curve so that it matched the venous blood sample activity level at late times and then multiplying the result by a population-based metabolite-fraction time–activity curve derived from the original cohort. The parent ^{18}F-FDHT input function could then be calculated by subtracting this metabolite input function from the scaled population-based blood time–activity curve (Fig. 2).

Pharmacokinetic Modeling

A series of linear compartmental pharmacokinetic models of increasing complexity were tested on the tumor tissue data and compared using the Bayesian information criterion (BIC) as formulated by Schwartz (*7*). The definition of BIC is given as

$$\mathrm{BIC} = n\ln\left(\frac{\mathrm{RSS}}{n}\right) + k\ln(n),$$

where n is the number of data points, RSS the residual sum of squares from the estimated model, and k the number of free parameters used in the model fit.

The BIC provide a statistical metric with which to compare the results of different model fits to the data. The model yielding the lowest BIC value is judged to be of sufficient dimension (i.e., have enough parameters) to describe the data. The BIC increase as a function of the residual sum of squares of the fitted data, but they also increase as the number of model parameters used to fit the data is increased. In this way, the introduction of more than a requisite number of compartments is penalized. Hence, lower BIC imply either fewer explanatory variables, better fit, or both.

The patient data were fitted to 4 different compartmental models that were then compared using the BIC metric. These models are diagrammed in Figure 3. The first and simplest of these models, model 1, consisted of an instantaneously equilibrating space (often also referred to as a fractional blood volume), followed by a unidirectional trap, thus requiring just 2 parameters. The instantaneously equilibrating space was assumed to contain both parent ^{18}F-FDHT and its metabolites, whereas the trap was assumed to contain only parent ^{18}F-FDHT. The exclusion of the metabolites from the final compartment was justified on the basis of our in vitro studies demonstrating that the radiolabeled metabolites of ^{18}F-FDHT do not bind to CWR22-rv1 cells.

The next 2 models (2a and 2b) are similar to the first model except for the addition of a reversible space between the instantaneously equilibrating space and the trap. The 2 variants differed in their exclusion (2a) and allowance (2b) of metabolites into this intermediate space. When allowed, the metabolites were forced to enter and exit this space using rate constants constrained to equal that of the parent ^{18}F-FDHT; thus, each of the 2 variants required 4 parameters. We chose to equate these rate constants under the assumption that the associated space represents a region of disrupted vasculature into which radiolabeled molecules bound to plasma proteins were leaking. For the most complex model tried, model 3, an additional reversible space preceding the unidirectional trap was added, requiring a total of 6 parameters. In this model, metabolites were allowed to enter the first reversible space (again using rate constants constrained to equal that of ^{18}F-FDHT) but not allowed to enter the second.

In each of these models, we have assumed that the entirety of the parent ^{18}F-FDHT in the blood is equally available for uptake into the tumor, whether it is bound to plasma proteins or to steroid hormone–binding globulin or other constituents of the blood or free in the plasma. Therefore, our input functions are based on whole-blood activity concentrations.

The ^{18}F time–activity data for each lesion in each patient PET study was independently fitted by each of the described model variants using the SAAM II software package (University of Washington). Parameter values were adjusted to minimize the sum of the weighted squared differences between the model estimate and the corresponding measured values. The weight for each PET time point was chosen to be the inverse of the duration of its frame. The parent ^{18}F-FDHT and metabolite input functions applied to the models were the individually scaled population-based curves as described above. BIC values for each of the fits were calculated by SAAM II.

RESULTS

Clinical Image Data

Thirteen patients were studied in this protocol. Most of the metastatic sites were in bone. A summary of the patient scans and treatment regimens is provided in Table 1. A detailed description of these scans is beyond the scope of this article. However, in brief, several of these patients exhibited concordant PET lesion detection by ^{18}F-FDHT and ^{18}F-FDG PET, with patient 12 showing ^{18}F-FDG positivity and ^{18}F-FDHT negativity and patient 4 exhibiting only abnormal ^{18}F-FDHT uptake. Two of the patients (12 and 13) did not demonstrate ^{18}F-FDHT uptake in any

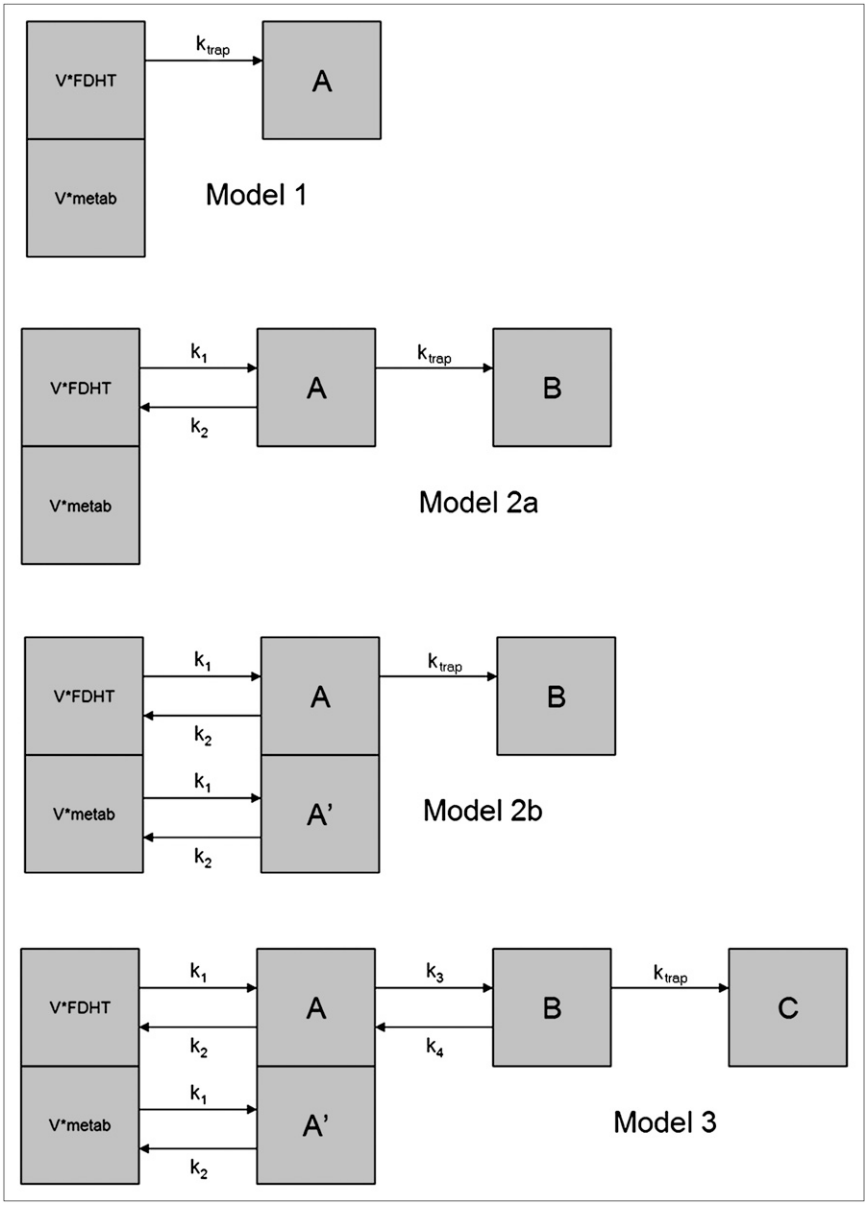

FIGURE 3. Four compartmental models used to fit ^{18}F-FDHT data to tumor uptake profiles. V*FDHT = volume time FDHT concentration; V*metab = volume times metabolism concentration.

tumors and were, thus, excluded from further analysis. Some of the patients demonstrated mixed findings between the SUVs measured for corresponding lesions, with high SUV on ^{18}F-FDG and low SUV on ^{18}F-FDHT scans, or vice versa. Most patients with positive ^{18}F-FDHT baseline scan findings exhibited uptake on posttherapy scans at reduced levels. However, there were instances of increased uptake on the follow-up ^{18}F-FDHT PET scans, for example, patient 1. One patient (patient 10) had multiple positive lesions on the baseline ^{18}F-FDG scan and a negative baseline ^{18}F-FDHT scan result but new abnormal ^{18}F-FDHT uptake in these regions on the later PET scans. Although several of the patients had some soft-tissue areas of abnormal ^{18}F-FDG uptake without corresponding ^{18}F-FDHT uptake, patient 7 showed abnormal ^{18}F-FDG and ^{18}F-FDHT uptake in lymph nodes in the left neck and retroperitoneum, with increasing ^{18}F-FDHT uptake on subsequent scans.

From this patient cohort in Table 1, the following values are observed: the average age of the patients was 66.7 y, with a range of 49–79 y. The median prostate-specific antigen value was 94.65, with a minimum of 0.49 and a maximum of 885.05. The average Gleason score for these patients was 7, with a range of 5–10. The Karnofsky performance status (KPS) values were either 80 (6 patients) or 90 (7 patients). Nine patients had bone disease, 8 had visceral or lymph node lesions, and 4 had both bone and visceral or lymph node disease.

Metabolite Analysis

There was no free ^{18}F-FDHT, as determined by size-exclusion filtration of serum samples. Recovery of ^{18}F

TABLE 1. Summary of Patient Scans and Treatment Regimens

Patient no.	Age (y)	Prostate-specific antigen at baseline	Gleason score	KPS	No. of PET scans	Site of disease	Therapeutic regimen
1	65	885.05	9	80	3	Bone	Docetaxel (Sanofi-Aventis)
2	68	96.62	10	80	3	Bone, lymph node, prostatic mass, soft tissue	Docetaxel (Sanofi-Aventis)
3	75	10.44	5	90	1	Bone	17AAG (AG Scientific), docetaxel (Sanofi-Aventis)
4	73	24.90	7	90	3	Lymph node	Abiraterone (Cougar Biotechnology)
5	59	7.52	9	90	3	Bone, lymph node	Abiraterone (Cougar Biotechnology)
6	49	27.04	7	90	3	Lymph node	MDV3100 (Medivation, Inc.)
7	53	96.45	9	90	3	Bone, lymph node	17AAG (AG Scientific), docetaxel (Sanofi-Aventis)
8	74	47.22	7	80	2	Bone	Docetaxel (Sanofi-Aventis)
9	70	0.49	7	90	2	Bone	17AAG (AG Scientific), docetaxel (Sanofi-Aventis)
10	59	5.28	9	80	3	Liver	Docetaxel (Sanofi-Aventis)
11	76	10.42	6	90	2	Bone	Palliative radiotherapy to sacrum
12	67	17.51	10	80	1	Bone, lymph node, liver	5-Fluorouracil (Pharmacia and Upjohn), oxaliplatin (Sanofi-Aventis)
13	79	1.52	7	80	1	*	Bicalutamide (AstraZeneca)

*Reading for patient 13 had confidence of metastases of equivocal; therefore, sites of disease were not identified.

activity from the acetonitrile-precipitated serum samples was around 89% and showed no trend with increasing metabolite levels. A series of HPLC chromatograms for 1 patient study is shown in Figure 4. The earliest samples, obtained at 1 min after injection, show the activity eluting at 7.6 min as ^{18}F-FDHT. Later serum samples show increasing amounts of a metabolite eluting at 4 min. The serum count data and HPLC analysis data were combined to give a time–activity curve for total blood activity and ^{18}F-FDHT and radiolabeled metabolite levels (Fig. 5)

Compartmental Analysis

Twenty-six tumor time–activity datasets were fitted by each of the 4 compartmental models proposed. All datasets fit well to model 1; for 16 of the datasets, the BIC found model 1 to be of the most appropriate dimension. By these criteria, model 2a was most appropriate for 7 cases, and model 2b was best in 2 cases. However, in both of the cases for model 2b, the distribution volumes for the metabolites were found to be quite high (28% and 67%), possibly inconsistent with our in vitro findings that the metabolites

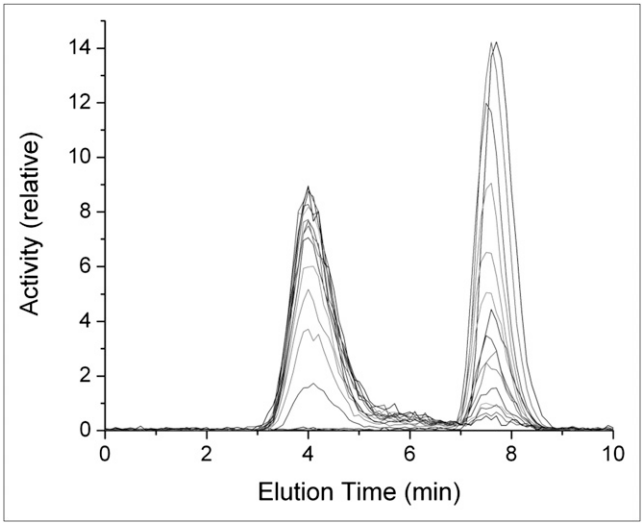

FIGURE 4. Series of HPLC elution profiles showing progressive decrease in ^{18}F-FDHT (retention time, 6.7 min) and increase in metabolites (retention time, 4.0 min).

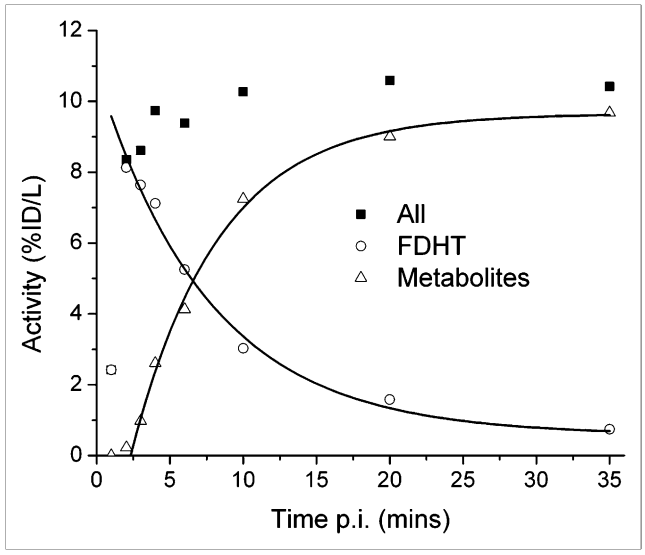

FIGURE 5. Time course of ^{18}F-FDHT and metabolite levels in serial patient sera. %ID/L = percentage injected dose per liter.

do not enter or bind to the cell membrane. The most complex model, model 3, was best by the BIC for only 1 dataset. In this case, the unidirectional rate constant k_{trap} went to zero.

As can be seen from the results shown in Table 2, the pattern of the model selection does not appear to correlate with individual tumors; that is, repeated studies of the same tumor yielded different models judged as the most appropriate. In the few cases in which either model 2b or model 3 was judged best, the BIC value was not substantially better (i.e., lower) than its values for models 1 and 2a, suggesting perhaps that their seeming superiority might be due to random correlations in the noise. Thus, we present parameter values for only models 1 and 2a in Table 2, leaving the description of models 2b and 3 results to the "Discussion" section. Also in Table 2 are the estimation of the fraction of the measured tumor tissue activity that is bound to AR at 30 min after injection and SUV at that time for models 1 and 2a. The correlation between the k_{trap} term and the 30-min SUV of model 1 is shown in Figure 6, suggesting the possibility of using a simplified imaging protocol that does not involve blood sampling or modeling.

Sample results of the compartmental modeling are presented in Figure 7A, which shows the fits for model 1 to the measured tumor time–activity data for ^{18}F-FDHT in patient 1. This patient underwent 1 pre- and 2 posttherapy ^{18}F-FDHT scans, and for all of these scans model 1 was selected by the BIC. The results consistently show what might be interpreted as a progressive reduction in AR concentration (or a reduction in AR-expressing viable cells) in response to therapy, but alternative interpretations cannot be ruled out on the basis of these data alone.

DISCUSSION

The objectives of this study were to define the pharmacokinetic properties of the tracer, determine the metabolism of ^{18}F-FDHT in blood, and determine whether the data could support a model having parameters that might prove to be correlated with AR concentration. The prospects for measuring a parameter correlated to AR concentration are founded on the assumption that the rate of ^{18}F-FDHT to AR binding is proportional to the product of the unbound concentrations of ^{18}F-FDHT and AR, for which the proportionality constant is the bimolecular association rate constant k_{on}. In compartmental modeling terms, this means identifying a rate constant that is equal to (or at least consistently proportional to) the product of k_{on} and the concentration of unbound AR (the latter of which is essentially a constant, given tracer levels of ^{18}F-FDHT). It was our goal in this study to ascertain the limits of our dynamic PET measurements in resolving model parameters that might prove to be so correlated.

Of the compartmental models tested, 2 were frequently chosen by the BIC as being most consistent with the available data. The first of these, model 1, fits reasonably well to all datasets. Model 1 is a simple 2-parameter model, with 1 parameter being the rate constant associated with a unidirectional trap (at least over the time period of these experiments) of ^{18}F-FDHT into the tumor. Thus, in model 1 the resultant k_{trap} term comprises a combination of intracellular transport and association with the binding domain. As a consequence, tumor-to-tumor (or tumor response) differences may be the result of changes in intracellular transport in addition to any change in AR concentration. For example, P-glycoprotein–mediated differences in the efflux of DHT between various tumor cell lines has been reported (*8*), differences that could be reflected in this rate constant.

The results for model 2a suggest that in some cases it may be possible to derive a parameter that is more directly related to the free AR concentration, but our results also suggest that the determination of this parameter is less robust. More robust was the determination of the composite parameter describing the steady-state net influx rate constant K_i, which in the case of model 2a is equal to $k_1k_{trap}/(k_2+k_{trap})$. The value for K_i was in general found to be close to the k_{trap} value of model 1. However, there were some cases in which the final trapping term, and thus K_i, went to zero. Although infrequent, this emphasizes that over the time frame of the current datasets (30 min) a significant portion of the measured PET signal might be due to the distribution of ^{18}F-FDHT into reversible precursor compartments—that is, upstream transport events rather than binding to AR.

Similar quality fits to the data can be obtained with models 1 and 2a (Figs. 7A and 7B, corresponding to different model fits to the same patient data), with associated differences in interpretation. Lower residuals were obtained with model 2a than with model 1, but according to the BIC the degree of improvement in the fit did not justify the additional parameters. This does not in and of itself mean that the model 2a interpretation is wrong, but rather its compartments merely cannot be reliably discriminated by these data. With this in mind, one would have to accept the possibility of the model 2a interpretation, in which there is little to no binding of ^{18}F-FDHT to AR in the tumor (Fig. 7B) at baseline and only moderate binding at 3 and 6 mo after therapy, compared with the perhaps more plausible interpretation, that of model 1, of progressive response to therapy.

To distinguish which of the foregoing scenarios is most likely, it is necessary to consider other relevant data. Evidence that ^{18}F-FDHT uptake is indeed measuring the binding of ^{18}F-FDHT to AR is provided by in vitro and in vivo blocking studies, the latter conducted in baboons (*2*). In the baboon study, ^{18}F-FDHT was coadministered with relatively high levels of nonradiolabeled testosterone, which was shown to reduce the amount of ^{18}F-FDHT uptake into the prostate. If we assume that the transport of ^{18}F-FDHT is not itself saturable, then the reduced uptake is most likely explained by a reduction in free AR because of its binding to testosterone-derived DHT. This same study

TABLE 2. Pattern of Model Selection

Patient no.	Scan	Tumor	Model (BIC values)				Model 1 parameter values			Model 2a parameter values						SUV_{bw} maximum 30 min after injection
			1	2a	2b	3	V	k_{trap}	Bound fraction	V	k_1	k_2	k_{trap}	K_i	Bound fraction	
1	Before	1	***1.20***	1.27	1.29	1.29	0.050 (0.031)	0.115 (0.004)	0.95	0.033 (0.032)	0.126 (0.008)	0.004 (0.003)	0.000 (0.000)	0.000	0.00	8.0
1	After 1	1	***0.94***	1.03	1.02	1.17	0.027 (0.029)	0.074 (0.004)	0.96	0.000 (0.000)	0.199 (0.237)	1.507 (4.246)	0.952 (0.994)	0.077	0.99	4.5
1	After 2	1	***0.32***	0.42	0.51	0.65	0.001 (0.015)	0.037 (0.002)	1.00	0.000 (0.000)	0.042 (0.007)	0.015 (0.041)	0.078 (0.211)	0.035	0.78	2.3
2	Before	1	***2.16***	2.29	2.28	2.43	0.042 (0.066)	0.120 (0.009)	0.96	0.000 (0.000)	0.237 (0.347)	0.763 (3.779)	0.829 (1.783)	0.124	0.99	11.2
2	After	1	1.35	***1.28***	1.37	1.52	0.010 (0.035)	0.096 (0.005)	0.99	0.000 (0.000)	0.138 (0.023)	0.073 (0.074)	0.154 (0.102)	0.093	0.93	6.8
3	Before	1	2.09	***1.29***	1.86	2.00	0.185 (0.090)	0.036 (0.011)	0.63	0.000 (0.000)	0.166 (0.017)	0.080 (0.016)	0.018 (0.006)	0.031	0.47	3.3
4	Before	1	0.88	0.91	***0.77***	0.83	0.027 (0.006)	0.090 (0.002)	0.97	0.017 (0.010)	0.139 (0.051)	0.259 (0.507)	0.467 (0.506)	0.089	0.96	6.6
4	Before	2	***1.78***	1.87	1.83	1.80	0.054 (0.022)	0.063 (0.005)	0.91	0.025 (0.047)	0.210 (0.292)	0.828 (2.228)	0.364 (0.382)	0.064	0.93	5.5
4	After	1	***1.10***	1.25	1.22	1.33	0.045 (0.018)	0.103 (0.004)	0.95	Collapsed to model 1						5.5
4	After	2	***1.04***	1.15	1.21	1.31	0.138 (0.032)	0.070 (0.005)	0.81	0.125 (0.037)	0.083 (0.022)	0.013 (0.044)	0.032 (0.216)	0.058	0.41	4.5
5	After	1	***0.71***	0.79	0.84	0.98	0.054 (0.014)	0.054 (0.003)	0.90	0.040 (0.020)	0.100 (0.068)	0.304 (0.775)	0.360 (0.478)	0.054	0.90	3.1
5	After	2	***0.60***	0.74	0.64	0.81	0.111 (0.020)	0.055 (0.003)	0.81	Collapsed to model 1						3.3
5	After	1	***0.61***	0.67	0.78	1.20	0.000 (0.019)	0.078 (0.003)	0.81	0.000 (0.000)	0.09 (0.003)	0.01 (0.002)	0.00 (0.000)	0.000	0.90	4.5
5	After	2	***0.90***	0.94	1.10	1.80	0.005 (0.005)	0.026 (0.002)	0.81	0.000 (0.000)	0.05 (0.011)	0.11 (0.014)	0.12 (0.014)	0.024	0.90	1.6
6	Before	1	***1.55***	1.70	1.77	1.92	0.267 (0.032)	0.074 (0.005)	0.70	Collapsed to model 1						10.1
6	Before	2	***1.25***	1.28	1.44	1.58	0.200 (0.017)	0.094 (0.003)	0.80	0.189 (0.018)	0.106 (0.010)	0.008 (0.015)	0.012 (0.129)	0.062	0.19	11.0
6	Before	3	***1.67***	1.81	1.76	1.89	0.227 (0.041)	0.059 (0.006)	0.69	Collapsed to model 1						8.1
7	After 2	1	2.28	***1.64***	1.73	2.18	0.179 (0.101)	0.120 (0.014)	0.85	0.002 (0.055)	0.276 (0.032)	0.073 (0.022)	0.045 (0.016)	0.106	0.71	8.2
8	Before	1	1.13	***0.17***	0.80	0.94	0.057 (0.031)	0.054 (0.004)	0.89	0.006 (0.012)	0.092 (0.006)	0.035 (0.009)	0.022 (0.014)	0.036	0.43	3.5
8	After	1	1.78	***1.62***	1.79	1.94	0.000 (0.000)	0.183 (0.003)	1.00	0.000 (0.000)	0.241 (0.026)	0.040 (0.032)	0.097 (0.062)	0.170	0.86	11.5
9	Before	1	***1.71***	1.83	1.78	1.92	0.080 (0.042)	0.032 (0.006)	0.77	0.065 (0.046)	0.041 (0.012)	0.013 (0.013)	0.000 (0.000)	0.000	0.00	3.1
9	After	1	1.79	***1.17***	1.45	1.59	0.093 (0.050)	0.041 (0.007)	0.79	0.000 (0.000)	0.209 (0.037)	0.381 (0.129)	0.109 (0.021)	0.046	0.91	4.1
10	Before	1	***1.74***	1.88	1.85	1.99	0.009 (0.043)	0.036 (0.006)	0.97	0.004 (0.048)	0.039 (0.012)	0.005 (0.014)	0.000 (0.000)	0.000	0.00	3.1
10	After	1	1.99	1.98	2.04	***1.96***	0.119 (0.054)	0.088 (0.007)	0.86	0.077 (0.052)	0.115 (0.014)	0.014 (0.005)	0.000 (0.000)	0.000	0.00	7.9
11	Before	1	1.49	***1.03***	1.60	1.19	0.063 (0.029)	0.070 (0.004)	0.90	0.022 (0.019)	0.100 (0.009)	0.022 (0.012)	0.021 (0.031)	0.048	0.38	7.2
11	After	1	1.18	1.09	***1.05***	1.19	0.153 (0.032)	0.031 (0.004)	0.63	0.053 (0.066)	0.290 (0.306)	1.444 (1.695)	0.236 (0.066)	0.041	0.84	3.2
12*	Before	1														
13*	Before	1														

*No ^{18}F-FDHT uptake was observed for patients 12 and 13; therefore, these patients were excluded from further analysis.

Units for k_{trap}, k_1, k_2, and K_i are all 1/min. V parameters are unitless, as are bound fraction and SUV normalized by body weight; (SUV_{bw}). Bolded and italicized BIC values are minimums. Values in parentheses are SD. Before = before therapy; after = after therapy.

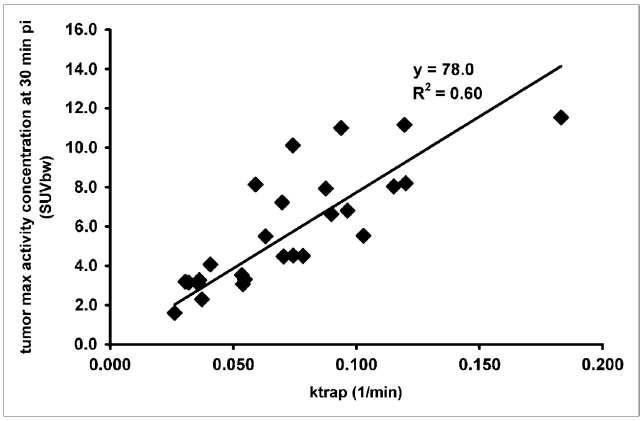

FIGURE 6. Scattergram showing relationship between k_{trap} parameter values calculated in model 1 with 30-min SUV. These data are fitted with line forced through origin. SUV_{bw} = SUV normalized by body weight.

also showed a loss of ^{18}F-FDHT from baboon prostate after about 3 h, perhaps from a slowly equilibrating compartment but also possibly due to reversible binding of ^{18}F-FDHT to AR. Furthermore, biopsy samples from lesions positive for ^{18}F-FDHT also stained positively for AR by immunohistochemistry (*5*).

Although significant questions remain regarding the potential of ^{18}F-FDHT to directly measure free AR concentration, taken together the results of this and other studies suggest the potential that clinically useful information may be provided from net uptake parameters such as the k_{trap} of model 1 or the K_i of model 2. Indeed, this parameter may be more useful clinically, because it is the binding of the AR–testosterone complex to androgen response elements on the DNA that affects gene expression (*8*), not AR expression levels per se.

Caveats of our analysis included our inability to obtain input functions from arterial blood sampling (which would impede patient accrual and limit protocol utility). Because most patients did not have lesions close to the heart, we—for the time being—overcame this limitation through the use of a population-derived input function (derived from the aorta ROIs of 25 patients) for modeling. The parent ^{18}F-FDHT input function was then calculated by subtracting the metabolite input function (determined from venous blood samples) from the scaled population-based blood time–activity curve, as shown in Figure 2. In general, the high rate of ^{18}F-FDHT metabolism is a difficulty in that it gives rise to what is in effect a second input function resulting from the recirculation of the radiolabeled metabolites into the blood. However, our metabolite analysis showed that the ^{18}F species appears to be tightly bound to plasma proteins and thus remains in the blood compartment. Whereas egress of these metabolites into the interstitium cannot be ruled out, we have demonstrated by in vitro studies with CWR22 cell lines that these metabolites do not bind to AR.

CONCLUSION

Independent of these difficulties, the success of model 1 in fitting the tumor time–activity curves suggests the potential for simpler acquisition protocols involving a static PET measurement with and without a simultaneous venous blood sample. As described here and in a previous publication from our group (*5*), the metabolism of ^{18}F-FDHT is such that the parent compound is almost entirely eliminated from the blood by 15 min. After this time, the area under the input function curve increases by less than

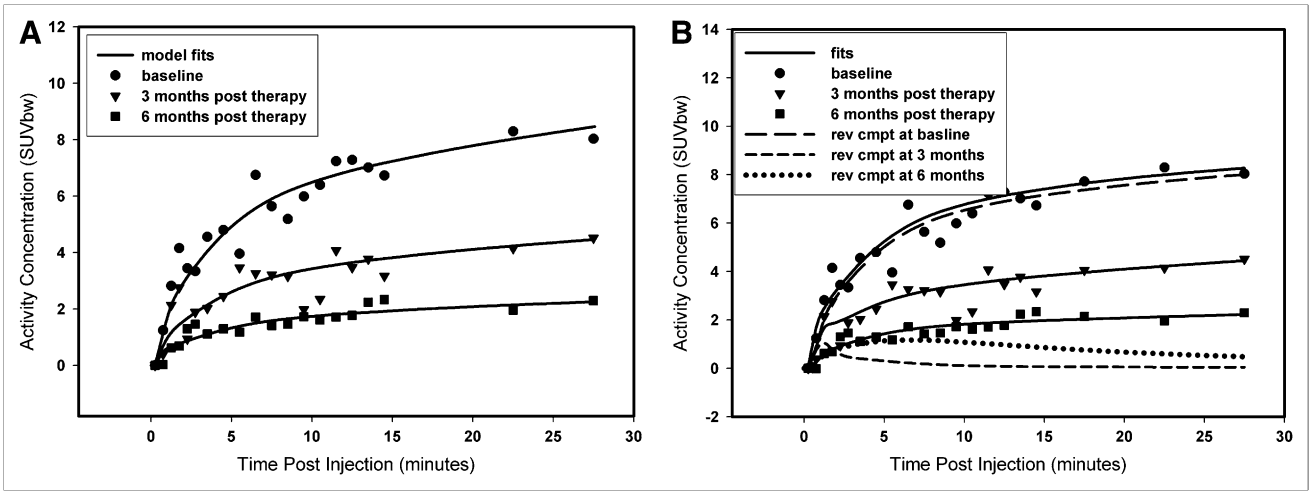

FIGURE 7. (A) Tumor time vs. activity concentration data for 3 studies (1 pretherapy and 2 posttherapy) of patient 1 fitted with model 1. (B) Same 3 datasets as in A, this time fitted by model 2a. Time course of modeled reversible compartment for each of these is also shown. SUV_{bw}= SUV normalized by body weight; Rev cmpt = reversible compartment.

1% per minute. This finding, coupled with an assumption of rapid equilibration of any reversible spaces within the model, gives rise to a system in which the PET tumor activity measurement rapidly reaches a plateau confounded primarily by metabolites whose concentration is proportional to the metabolite level in the blood. If we assume a reasonable value for this proportionality constant, then an offset correcting the measured tumor activity concentration for metabolites can be estimated. The activity in the blood sample would also be used to scale the area under the population–based ^{18}F-FDHT input curve. The metabolite-corrected tumor tissue value divided by the scaled area under the curve is then equal to k_{trap}. If the contribution of the metabolites to the tumor tissue measurement is small, then a simple SUV-type measure may suffice.

In the future, we plan further validation of our simplified approach by testing the correlation of ^{18}F-FDHT SUV (>15 min after injection) with histologic AR staining intensity and by testing the correlation of changes in SUV with measures of clinical outcome. We also hope to modify the formulation of the injectate to avoid the problems with injection and therefore input function variability.

ACKNOWLEDGMENTS

This work was supported by the Memorial Sloan-Kettering Center grants P50-CA92629 ("SPORE in Prostate Cancer"), P50 CA086438 ("In Vivo Center for Molecular and Cellular Imaging"), and K23: CA102544.

REFERENCES

1. Chen Y, Sawyers CL, Scher HI. Targeting the androgen receptor pathway in prostate cancer. *Curr Opin Pharmacol.* 2008;8:440–448.
2. Choe YS, Lidström PJ, Chi DY, Bonasera TA, Welch MJ, Katzenellenbogen JA. Synthesis of 11 β-[^{18}F]fluoro-5 α-dihydrotestosterone and 11 β-[^{18}F]fluoro-19-nor-5 α-dihydrotestosterone: preparation via halofluorination-reduction, receptor binding, and tissue distribution. *J Med Chem.* 1995;38:816–825.
3. Bonasera TA, Oneil JP, Xu M, et al. Preclinical evaluation of fluorine-18-labeled androgen receptor ligands in baboons. *J Nucl Med.* 1996;37:1009–1015.
4. Dehdashti F, Picus J, Michalski JM, et al. Positron tomographic assessment of androgen receptors in prostatic carcinoma. *Eur J Nucl Med Mol Imaging.* 2005;32:344–350.
5. Larson SM, Morris M, Gunther I, et al. Tumor localization of 16β-^{18}F-fluoro-5α-dihydrotestosterone versus ^{18}F-FDG in patients with progressive, metastatic prostate cancer. *J Nucl Med.* 2004;45:366–373.
6. Zanzonico PB, Finn R, Pentlow KS, et al. PET-based radiation dosimetry in man of ^{18}F-fluorodihydrotestosterone, a new radiotracer for imaging prostate cancer. *J Nucl Med.* 2004;45:1966–1971.
7. Schwartz G. Estimating dimension of a model. *Ann Stat.* 1978;6:461–464.
8. Fedoruk MN, Gimenez-Bonafe P, Guns ES, Mayer LD, Nelson CC. P-glycoprotein increases the efflux of the androgen dihydrotestosterone and reduces androgen responsive gene activity in prostate tumor cells. *Prostate.* 2004;59:77–90.